ROYAL SOCIETY OF CHEMISTRY

PAPER

Check for updates

Anisotropic X-ray detection performance of melt-grown CsPbBr₃ single crystals†

Yunqiu Hua,‡ Xue Sun,‡ Xiang Li, Fucai Cui, Zhongjie Yue, Jiaxin Liu, Hongjie Liu, Guodong Zhang* and Xutang Tao 🆔 *

All-inorganic perovskite CsPbBr₃ has been regarded as a new semiconductor radiation material with great potential due to its excellent carrier transport performance and thermal stability. However, it remains challenging to optimize the size and quality of CsPbBr₃ single crystals for commercial applications. Here, the [100], [010], and [001] orientations of bulk CsPbBr₃ single crystals were examined, and their anisotropic X-ray detection performance was investigated. The regular positive and negative charge distributions at the outer (010) surface and the connection of $[PbBr_6]^{4-}$ octahedrons with the [010] orientation contribute to decreased defect densities and enhanced carrier transportation of the (010) facet. Additionally, the wafer with the [010] orientation exhibited the weakest ion migration among the three orientations due to the largest active energy (143.77 meV) and ion diffusion barrier energy (0.361 eV), which is advantageous for enhancing the X-ray response. Moreover, the (010) CsPbBr₃ single crystal detector, which was fabricated with EGaIn and Au electrons, demonstrated the maximum sensitivity of 34 449 $\mu C\ Gy_{air}^{-1}\ cm^{-2}$ under a high bias voltage of −400 V and the lowest detection limit of 52.6 $nGy_{air}\ s^{-1}$ compared with the other two devices. This work highlights the anisotropic engineering of large-size single crystals for boosting perovskite radiation performance and provides valuable advice for the oriented growth of large-size crystals and films.

State Key Laboratory of Crystal Materials, Institute of Crystal Materials, Shandong University, Jinan 250100, P. R. China. E-mail: zgd@sdu.edu.cn, txt@sdu.edu.cn

† Electronic supplementary information (ESI) available. See DOI: **https://doi.org/10.1039/d3tc01085f**

‡ These authors contributed equally to this work.

Guodong Zhang

Guodong Zhang is a full professor at the Institute of Crystal Materials, Shandong University. He received his PhD degree in 2012 under the supervision of Prof. Xutang Tao at Shandong University. From 2013 to 2015, he worked on his postdoctoral research on the solvo-thermal synthesis of novel chalcogenide crystals and liquid-phase epitaxy (LPE) growth of novel nitride single crystals at Nanyang Technological University's Materials Science Division and National Institute for Materials Science, respectively. His current research interest is focused on the growth of metal halide bulk single crystals for radiation detection and infrared detection applications.

1. Introduction

X-ray detection has been widely applied in nondestructive inspection, medical imaging, astrophysics, and scientific research.[1–3] Compared with scintillation detectors, semiconductor detectors directly convert X-ray energy into electrical signals, and therefore, they exhibit considerable potential for high resolution and rapid response. Among all semiconductor X-ray detectors, the ability of Si to absorb X-rays is weak, and its transportation performance is poor.[4] Similarly, it is expensive to grow single crystals of CdTe and CdZnTe (CZT) for device operation.[3,5,6] Therefore, it is necessary to explore new semiconductor materials with high detection performance and low cost.

Lead halide perovskite materials have been developed over the past few decades, and they currently exhibit outstanding performance in solar cells,[7] photodetectors,[8] light-emitting diodes (LEDs),[9] lasers,[10] and nuclear radiation detectors[1,2,11,12] because of their large average atomic number, tunable bandgap, and high mobility-lifetime ($\mu\tau$) products as well as relatively high resistivity.[13,14] In particular, all-inorganic lead halide perovskite CsPbBr₃ is useful in radiation detection due to its superior photoelectric properties, as well as satisfactory thermal and moisture stability.[10] There is a smaller leak current for a single crystal (SC) of CsPbBr₃, which results in high purity in

This journal is © The Royal Society of Chemistry 2023

J. Mater. Chem. C, 2023, **11**, 9153–9160 | **9153**

materials, a free grain boundary, and more optimal carrier transport properties compared with polycrystalline perovskite thin films and nanocrystals.[15,16]

Recently, Kanatzidis *et al.* reported a high-energy resolution of 1.4% for [137]Cs 662 keV γ-ray irradiation based on the CsPbBr$_3$ SC, which is comparable with the CZT detector. Hence, the CsPbBr$_3$ SC is regarded as one of the new-generation high-energy nuclear radiation detectors.[10] Toufanian *et al.* reported on the growth of a large-size CsPbBr$_3$ SC for γ-ray detection with a high-energy resolution of 2% at 662 keV for ^{137}Cs,[17] which further verifies its excellent nuclear irradiation performance.

In addition to γ-ray detection, a spectrometer-grade melt-grown CsPbBr$_3$ detector was applied for X-ray detection, whose sensitivity varied between a few tens to over 8000 μC Gy$_{air}^{-1}$ cm^{-2}, and the detectable dose rate was as low as 0.02 nGy$_{air}$ s^{-1}.[18] Moreover, the CsPbBr$_3$ SC detector demonstrated high potential in X-ray photo-counting applications for medical diagnostics, with high energy response linearity, high energy resolution, large count rate, and negligible polarization.[19] Nonetheless, the commercial applicability of CsPbBr$_3$ remains hampered by the inability to grow large-size SCs and the difficulties with optimization of the detection performance.

The anisotropy of SC perovskite has a relative impact on the transport of charge carriers and the optoelectronic properties according to the orientation of the atoms in the crystal lattice.[15,20–22] Therefore, exploring the anisotropic properties of perovskite SCs is one of the most efficient methods to enhance detection performance. Some groups have reported the anisotropy of tetragonal MAPbI$_3$ and cubic MAPbBr$_3$ hybrid perovskite SCs. The (110) plane in the MAPbI$_3$ SC exhibited low defect densities due to the orientations of the MA$^+$ dipoles and the stacking of [PbI$_6$]$^{4-}$ octahedrons, which decreased the dark current and increased the photocurrents.[23] Compared with the (100) facet, there was higher ionic conductivity and larger optical current in the (111) facet in the MAPbBr$_3$ SC, in which the MA$^+$ and Br$^-$ ion density was higher.[24]

CsPbBr$_3$ crystallizes as an orthorhombic structure with a *Pnma* space group at room temperature. Therefore, CsPbBr$_3$ single crystals will exhibit intense anisotropic optoelectronic properties. Dong *et al.* precisely fabricated (100) and (111) surface anisotropy of CsPbBr$_3$ single crystals and demonstrated that the carrier mobility of the (100) facet was up to 241 μm^2 V^{-1} s^{-1} higher than that of the polar (111) facet, due to lower surface defect density.[7] Our group investigated the optoelectronic anisotropy of bulk CsPbBr$_3$ SC and showed that there was a more optimal photoresponse from the (001) plane with [010] orientation. The radiation detection performance of bulk CsPbBr$_3$ SC in the regions of parallel and vertical growth direction was significantly different.[17] However, the relationship between the crystallographic orientations and the high-energy radiation detection performance of CsPbBr$_3$ SCs is rarely explored.

In this work, we report a large CsPbBr$_3$ SC with the size of Φ 36 mm × 50 mm grown using a modified vertical Bridgman (VB) method. The bulk CsPbBr$_3$ single crystals were orientated, and the (100), (010), and (001) wafers were polished for device fabrication. The structural anisotropy of CsPbBr$_3$ demonstrates a low defect density and great charge carrier transport in the (010) facet. Moreover, compared with others, the higher activation energy and ion diffusion barrier indicates a weaker ion migration of the wafer with [010] orientation. Hence, the (010) detector achieved an optimal sensitivity of 34 449 μC Gy$_{air}^{-1}$ cm^{-2} under a high bias voltage of −400 V and a detection limit of 52.6 nGy$_{air}$ s^{-1} for 120 keV X-ray detection. This work aims to explore the crystal facet with optimal properties that is conducive to the directional growth of large-size crystals and the optimization of X-ray detection performance.

2. Experimental section

2.1. Single crystal growth and wafer processing

High-purity CsBr (5 N) and PbBr$_2$ (5 N) were purchased from Aladdin Chemistry Co., Ltd and loaded in a silica ampoule that was subjected to a vacuum of 4 × 10^{-4} Pa, and was subsequently sealed with an oxyhydrogen flame. The above ampoule containing the raw materials was placed in a pit furnace that was equipped with a temperature controller (FP23, Shimaden, Japan). Usually, the temperature program of the pit furnace is divided into three steps. In the first step, the furnace is heated from room temperature to 600–700 °C at a rate of 60–70 °C h^{-1}. Then, the temperature is held for 24 h. Finally, the furnace is slowly cooled to room temperature at a rate of 20 °C h^{-1}. Polycrystalline CsPbBr$_3$ was then obtained for the growth of CsPbBr$_3$ single crystals.

CsPbBr$_3$ single crystals were grown in a homemade dual-temperature zone vertical Bridgman furnace that was reported in our previous work. The upper zone and lower zone of the furnace were set to approximately 640 °C and 300 °C, respectively, and the temperature gradient near the solid–liquid interface was approximately 12 °C h^{-1}. After placing the quart ampoule with the CsPbBr$_3$ polycrystals in the Bridgman furnace, the ampoule was maintained at approximately 640 °C for 6 h to completely melt the polycrystals. Afterward, the ampoule was slowly moved down to the lower zone, at the rate of 0.2 mm h^{-1}. The furnace was cooled to room temperature at the speed of 10–20 °C h^{-1} after the crystallization.

The as-grown CsPbBr$_3$ single crystals were oriented and cut into wafers with sizes of 4 mm × 4 mm × 1.5 mm using an STX-202A diamond wire-cutting machine. The surfaces of the wafers were polished using a 7000 mesh SiC sandpaper with acetone for lubricating. After polishing, the wafers were immersed in an HBr solution for approximately 60 s to reduce the degree of surface defects. Then, the surface of the sample was washed with toluene to remove the HBr residue.

2.2. Property characterization

X-ray diffraction (XRD) patterns of SC samples were measured using an AXS D8 AD-VANCE X-ray diffractometer (Bruker, MA, USA) with Cu Kα irradiation (λ = 1.54056 Å) in the range of 10°–90° (2θ) and scanning speed of 0.04 s per step.

9154 | *J. Mater. Chem. C*, 2023, **11**, 9153–9160

This journal is © The Royal Society of Chemistry 2023

2.3. Calculation method

First-principles calculations were carried out using density functional theory (DFT), as applied by the Vienna *ab initio* simulation package (VASP). The projector augmented-wave (PAW) technique was used, with a fixed 500 eV plane-wave kinetic energy cutoff. The energy criterion was set to 10^{-5} eV in the iterative solution of the Kohn–Sham equation. The Brillouin zone integration used a $2 \times 3 \times 2$ k-mesh. All the structures were relaxed until the residual forces on the atoms decreased to less than 0.02 eV Å^{-1}. The energy barriers for Br^- ion diffusion in the structures were calculated by the climbing image-nudged elastic band (CI-NEB) method.

2.4. Device fabrication and detector performance characterization

The Au electrode was sputtered on one side of the surface, and the EGaIn (Ga:60%; In:40%) electrode was coated on another of the $CsPbBr_3$ wafers. The size of the electrodes was 2×2 mm^2 within the square. The EGaIn/$CsPbBr_3$/Au asymmetric electrode structure was obtained for the evaluation of X-ray detector performance.

Current density–voltage (J–V) curves for the EGaIn/$CsPbBr_3$/Au devices were measured by an electric properties measurement system (Keithley 2450, Keithley Instruments, OH, USA) with the bias voltage from -400 to 400 V at various scan rates. Current–time (I–t) curves were measured by an electric properties measurement system (Keithley 6517B, Keithley Instruments, OH, USA).

A tungsten anode X-ray tube (VAREX RAD-14/Leo, Hamamatsu, Shizuoka, Japan) was used as the source with an X-ray beam limiter for 1×1 mm^2. The X-ray source was operated with an acceleration voltage of 120 keV. The dose rate was changed by adjusting the X-ray tube current from 10 to 25 mA, and the dose rate was calibrated using an X-ray machine multifunctional quality detector (Piranha 655, Piranha, Sweden). A source meter (Keithley 6517B, Keithley Instruments, OH, USA) was used to apply the bias voltage and record the response current. All measurements were performed at room temperature (25 °C) in air.

3. Results and discussion

3.1. Crystal growth and characterization

The growth of high-quality single crystals is of great significance for high-performance X-ray detectors. We adopted an optimized VB method to grow large-size $CsPbBr_3$ crystals. Fig. 1a exhibits a schematic diagram of the optimized semitransparent Bridgman furnace. The purification process for raw materials is crucial to the crystal. Fig. S1 (ESI†) shows the $CsPbBr_3$ polycrystalline ingots purified for the first time, and after the second and third time. The impurities were segregated into the end of the crystal due to the different segregation coefficients, which appeared as the black part at the end of the tube. These impurities might be the C, Cl, and Ca elements
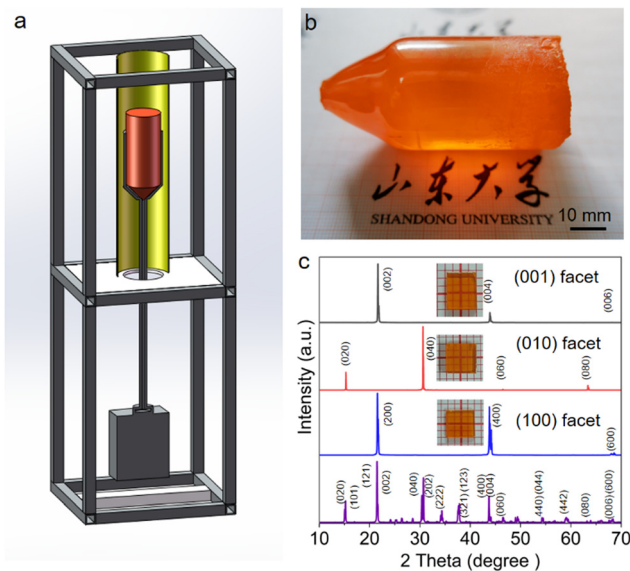

Fig. 1 (a) Schematic diagram of the vertical Bridgman furnace. (b) Photograph of an as-grown $CsPbBr_3$ single crystal. (c) XRD patterns of the (100), (010), and (001) wafers. The insets are photographs of the processed and polished wafers.

produced by the raw materials in the precursor synthesis process.[17]

In addition to purifying the raw materials, cracking must be prevented to obtain large-size $CsPbBr_3$ single crystals. When the temperature gradually decreases from the melting point to room temperature, the phase of $CsPbBr_3$ will change from cubic to tetragonal at 130 °C, and then to orthorhombic at 88 °C. The large thermal expansion coefficient near 130 °C usually results in a severe crack in $CsPbBr_3$ during the cooling process and reduces the quality of the crystal. When the cooling rate was decreased to 10–20 °C h^{-1}, there was less cracking. Fig. 1b shows as-grown $CsPbBr_3$ single crystals with the size of Φ 36 mm $\times$ 50 mm. After the bulk $CsPbBr_3$ SC was oriented, the crystal was processed into the (100), (010), and (001) wafers with a thickness of 1.5 mm. The photographs of the wafers in Fig. 1b demonstrate the satisfactory crystallization uniformity of the crystal. The X-ray diffraction (XRD) patterns confirmed the orientations of the wafers (Fig. 1c).

3.2. Structural anisotropy and charge carrier transport properties

The structure of the crystals, including the atomic arrangement, ion densities, and bond strengths, depends on the anisotropic properties. Fig. 2a–c exhibits the arrangement of the $[PbBr_6]^{4-}$ octahedrons for the (100), (010), and (001) facets of the $CsPbBr_3$ crystal, respectively. The arrangement of anions and cations at the outmost layers of the three facets is significantly different.[23] The Br^- ions are terminated at the outmost layers for the (100) and (001) planes, showing negative potentials at the surface of the wafers. For the (010) facet, the Br^- anions and Cs^+ cations are alternately stopped at the outermost layer, resulting in a charged equilibrium on the surface.

This journal is © The Royal Society of Chemistry 2023

J. Mater. Chem. C, 2023, **11**, 9153–9160 | **9155**

The relaxation and reordering of Br^- anions and Cs^+ cations at the terminal surface can diminish the surface energy, according to the Verwey theory.[25] Therefore, the arrangement of anions and cations that are terminated in the outmost layer of the (010) facet reduces the surface energy and inhibits defect recombination at the surface. Moreover, the various stacking arrangements of $[PbBr_6]^{4-}$ octahedrons for the (100), (010), and (001) facets lead to differences in charge transport properties along different orientations. As for the [100] and [001] orientations (Fig. 2a), there is an alternate array of the Cs^+ ions and $[PbBr_6]^{4-}$ octahedrons that forms zigzag chains and reduces the overlap of the Br-p orbital, which suppresses the charge transport. In contrast, continuous connections across $[PbBr_6]^{4-}$ octahedrons along the [010] orientation result in strong Br–Pb–Br bonds, which is beneficial for carrier transport.

A large mobility lifetime product ($\mu\tau$) increases the charge collection efficiency and improves detection performance. Fig. 2d–f compares the mobility lifetime products of the (100), (010), and (001) wafers, whose thicknesses were all 1.5 mm. The mobility lifetime products were obtained by fitting the obtained photocurrent curve with the modified Hecht equation:

$$I = \frac{I_0 \mu\tau V}{L^2} \frac{1 - \exp\left(-\frac{L^2}{\mu\tau V}\right)}{1 + \frac{Ls}{V\mu}} \quad (1)$$

where I_0 denotes the saturated photocurrent, L denotes the crystal thickness, V denotes the applied bias, τ denotes the carrier lifetime, and s denotes the surface recombination velocity. The $\mu\tau$ product of the [010] direction of 5.0×10^{-3} cm^2 V^{-1} is larger than that of the [100] (3.2×10^{-3} cm^2 V^{-1}) and [001] directions (3.1×10^{-3} cm^2 V^{-1}), which further validates the above theoretical model of carrier transport anisotropy in CsPbBr$_3$ crystals.

3.3. Anisotropic ion migration properties

It has been recognized that the strong ion migration under large electrical fields in perovskites degrades the performance of devices, leading to the drift of current. Because the migration of ions is strongly related to the structure of the crystal, it is essential to investigate the characteristics of ion migration along different orientations. To quantitatively understand the ionic migration in CsPbBr$_3$ SCs, the activation energies were calculated based on the temperature-dependent current–time curves for applying and removing bias voltages.[1]

A schematic of the typical charging–discharging process is shown in Fig. S2 (ESI†). A bias was applied on the device to promote the movement of ions, and these ions accumulated at the interface between the crystal and electrode. When the ions achieved stability, the bias was abruptly removed, and ions immediately began to travel backward as a result of the high concentration gradient, causing a negative current. As a result, the decay in the negative current curve can be used to evaluate the ion migration, and the activation energy can be fitted using the Arrhenius function from the I–t curves at various temperatures:

$$\ln k = C - \frac{E_a}{k_B T} \quad (2)$$

where k denotes the decay rate ($k = \tau^{-1}$), τ denotes the decay time, C denotes a constant, E_a denotes the ion activation energy for ion transport, k_B denotes the Boltzmann constant, and T denotes the absolute temperature. Fig. S3–S5 (ESI†) show the time-dependent dark currents after removing the bias. The τ values along the [100], [010], and [001] orientations were
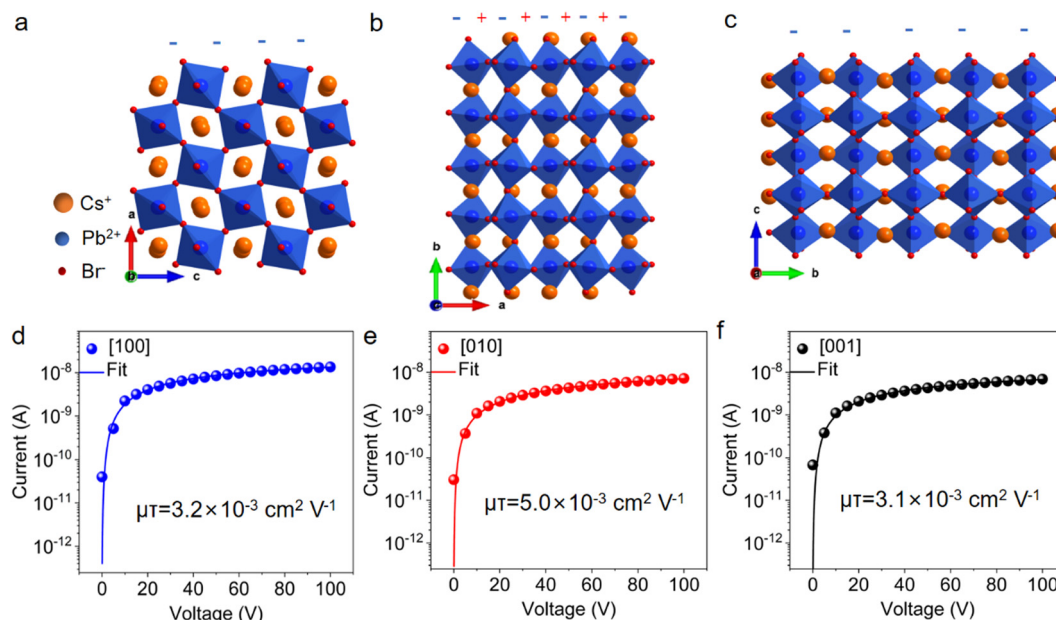

Fig. 2 (a–c) Arrangement of $[PbBr_6]^{4-}$ octahedrons in the CsPbBr$_3$ crystal structure, and (d–f) photocurrent fitting curves of the [100], [010], and [001] wafers of CsPbBr$_3$ crystal.

9156 | *J. Mater. Chem. C*, 2023, **11**, 9153–9160
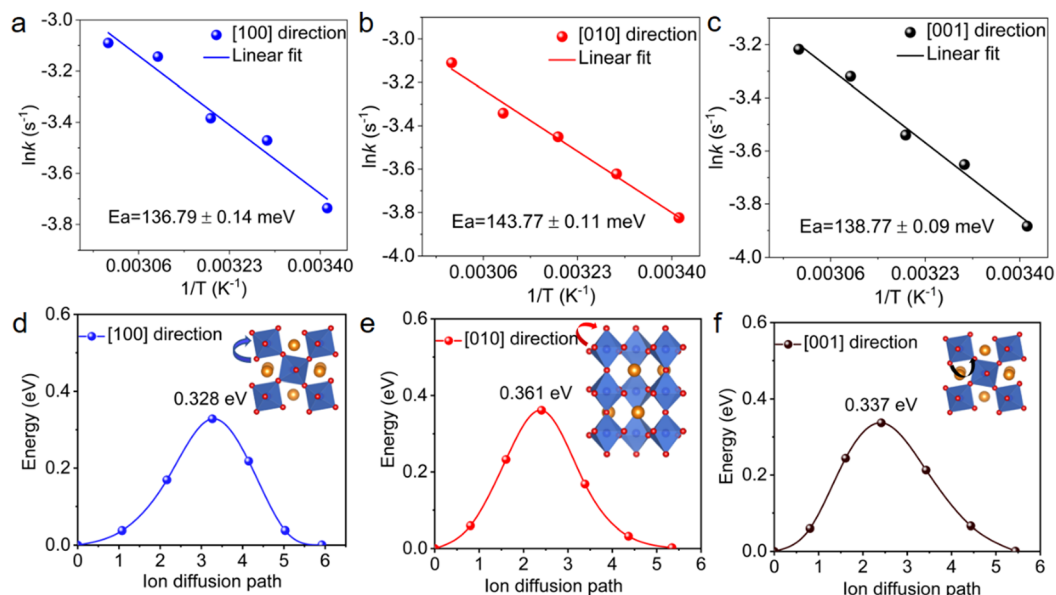
This journal is © The Royal Society of Chemistry 2023

Fig. 3 (a–c) Ion migration activation energies of $CsPbBr_3$ crystal wafers along the [100], [010], and [001] directions, respectively. (d–f) Calculated energy profiles of different ionic migration paths for Br^- ion vacancy along the [100], [010], and [001] orientations.

obtained by fitting curves using eqn (2) in the temperature range of 293–333 K. As shown in Fig. 3a–c, the active energy along the [010] orientation was calculated to be 143.77 meV, slightly larger than that along the [100] (136.79 meV) and [001] (138.77 meV) orientations. In the other words, compared with the [100] and [001] orientations, the higher diffusion barrier of ions that travel along the [010] orientation in $CsPbBr_3$ is beneficial for a higher performance device.

First-principles calculations were applied to investigate the anisotropy of ion migration in $CsPbBr_3$. Compared with Pb^{2+} and Cs^+ ions, the Br^- ion had the lowest activation energy in $CsPbBr_3$ due to the formation of Br^- ion vacancies.[26] The insets in Fig. 3d–f present the migration paths for the Br^- ion vacancy mechanism along the [100], [010], and [001] orientations. We chose a certain Br ion and calculated energy profiles along [100] (blue), [010] (red), and [001] (black) ionic migration channels. The diffusion barrier of the [010] orientation was calculated as 0.361 eV, which is higher than that of the [100] (0.328 eV) and [001] (0.337 eV) orientations.

This trend is consistent in our experiments, although the experimental results are less than the calculated values due to additional defects in actual crystals, which cause lower activation energy.[27] Therefore, the higher activation energy of the (010) wafer and the larger diffusion barrier energy along the [010] orientation demonstrated that there is weaker ion migration for the (010) wafer as compared to the others, which is meaningful for the optimization of the X-ray detection performance in $CsPbBr_3$ devices.

3.4. X-ray detection performance

A high electric field is generally required to enhance the charge collection efficiency and hence increase the sensitivity of the devices. However, the high electric field will result in the migration of ions, which deteriorates the stability of the detector. Fig. 4a schematically illustrates the architecture of the X-ray detector with a simple sandwich structure of EGaIn/$CsPbBr_3$ SC/Au. This asymmetric vertical device constructs a Schottky contact between the EGaIn and $CsPbBr_3$ SC under reverse bias, which decreases the dark current density under a high electrical field.

As shown in Fig. 4b, the current density–voltage (J–V) curves of the (100), (010), and (001) wafers based on the same part of the $CsPbBr_3$ SC demonstrated the rectifying characteristics. The (010) wafer presented a lower current density of 0.29 μA cm^{-2} as compared to those of the (100) wafer (0.36 μA cm^{-2}) and (001) wafer (0.58 μA cm^{-2}) under a bias at −400 V. Fig. 4c and Fig. S6 (ESI†) exhibit time-dependent X-ray responses under 120 keV X-ray photons, with dose rates ranging from 12.23 to 30.73 μGy$_{air}$ s^{-1} and bias from −10 to −400 V for the (010), (100), and (001) wafers, respectively. When the bias increased to −500 V, the detector demonstrated a severe baseline that was caused by ion migration, as shown in Fig. S7 (ESI†). The sensitivities were calculated using the equation:

$$S = \frac{I_{photo} - I_{dark}}{A \cdot R} \tag{3}$$

where I_{photo} and I_{dark} present the photocurrent and dark current for the device, respectively; R refers to the X-ray dose, and A denotes the effective area of the device.

As shown in Fig. 4d and Fig. S8 (ESI†), the X-ray photocurrent densities of the devices were linearly fitted to the dose rates under various bias voltages, and the sensitivities were calculated as 27 638, 34 449, and 28 421 μC Gy$_{air}$$^{-1}$ cm^{-2} under the voltage of −400 V for the (100), (010), and (001) detectors, respectively. Fig. 4e compares the whole sensitivities under different voltages for 120 keV X-ray photons. The sensitivities
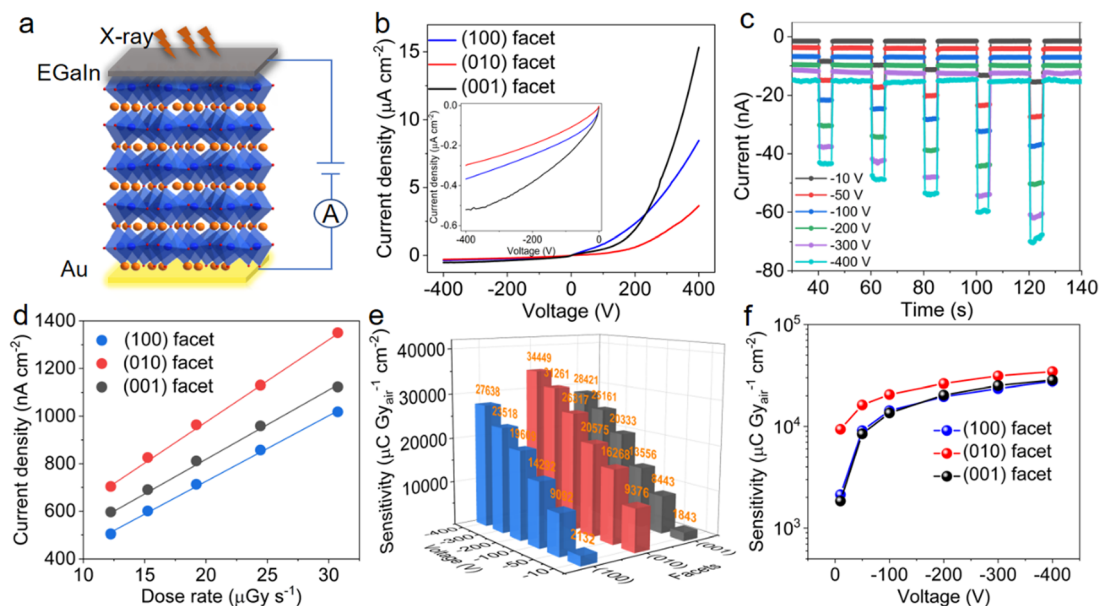
Fig. 4 (a) Schematic diagram of the CsPbBr$_3$ detector structure. (b) $J-V$ curves in dark from −400 V to 400 V. The inset shows the enlarged details from −400 V to 0 V. (c) Temporal X-ray responses of the device based on the (010) wafer under voltages from −10 V to −400 V. (d) Photocurrent response *via* dose rates at −400 V and (e and f) X-ray sensitivities of the (100), (010), and (001) wafers under different voltages.

of the (010) wafer were higher than those of the (100) and (001) wafers.

As the bias increased from −10 to −400 V, the sensitivities of the EGaIn/CsPbBr$_3$ SC/Au detectors gradually increased until saturation (Fig. 4f). The high electric field promotes the diffusion of charge carriers and improves the collection of charges. Once the voltage reaches a certain value, the photoinduced charges are completely collected so that there is saturation of the photocurrent.[28] The optimum value of 34 449 μC Gy$_{air}^{-1}$ cm^{-2} for the (010) detector under the highest bias at −400 V (corresponding to the electric field of −2666 V cm^{-1}) is due to the large $\mu\tau$ product and weak ion migration among the (100), (010), and (001) facets of a single crystal of CsPbBr$_3$. In addition, the sensitivity of the (010) facet detector is three orders of magnitude higher than that of commercial semiconductor α-Se (20 μC Gy$_{air}^{-1}$ cm^{-2})[2], and five times higher than that of the CZT detector (6069 μC Gy$_{air}^{-1}$ cm^{-2}).[29]

Compared with perovskite materials, the sensitivity value is one order of magnitude higher than that of the MAPbI$_3$ detector (1471.7 μC Gy$_{air}^{-1}$ cm^{-2})[30] and CsPbI$_3$ detector (2370 μC Gy$_{air}^{-1}$ cm^{-2}),[31] and two orders of magnitude higher than that of the FAPbI$_3$ detector (130 μC Gy$_{air}^{-1}$ cm^{-2})[32] and MAPbBr$_3$ detector (6169 μC Gy$_{air}^{-1}$ cm^{-2}).[33]

The current drift D was applied to investigate the stability of the detectors, which is calculated as:

$$D = (J_t - J_0)/(t \cdot E) \qquad (4)$$

where J_t and J_0 denote the current densities at the beginning and end points, respectively; E denotes the electric field; and t denotes the duration. As shown in Fig. 5a, all dark currents of detectors decreased with increasing time when they were maintained at 2000 s under a bias voltage of −10 V.

The calculated current drift of the (010) device was 9.36 × 10^{-2} pA cm^{-1} s^{-1} V^{-1}, which was lower than the (100) device (1.08 × 10^{-1} pA cm^{-1} s^{-1} V^{-1}) and (001) device (1.14 × 10^{-1} pA cm^{-1} s^{-1} V^{-1}), and demonstrated weaker ion migration in the [010] orientation of CsPbBr$_3$ SC than the [100] and [001] orientations. Additionally, the current drift of our CsPbBr$_3$ SC is three orders of magnitude smaller than that of other CsPbBr$_3$ SCs (14.9 pA cm^{-1} s^{-1} V^{-1}),[34] indicating that a high-quality SC exhibited more optimal performance.

The detection limit, which was defined as the dose rate with a signal-to-noise (SNR) value of 3, is another important parameter to use for evaluating the performance of the X-ray device. The SNR ratio of the device under various dose rates can be calculated, as follows:

$$\mathrm{SNR} = \frac{I_{\mathrm{photo}} - I_{\mathrm{dark}}}{\sqrt{\dfrac{\sum\limits_{i}^{n}\left(I_i - I_{\mathrm{photo}}\right)^2}{N}}} \qquad (5)$$

where I_{photo} denotes the average photocurrent, I_{dark} denotes the average dark current, and I_i denotes the generated photocurrent. Fig. 5b–d displays the X-ray responses of the (100), (010), and (001) wafer detectors at −10 V under 120 keV X-ray photons. A 2 mm-thick lead plate was inserted between the detector and the X-ray source to attenuate the dose rates to 135–260 nGy$_{air}$ s^{-1}. The current of the (010) device is larger than that of the (100) and (001) devices because there is a slower decrease of the current under the same period. Additionally, the SNR values increase with the increasing dose rates. Moreover, the SNR values of the (010) detector for the response to the X-ray with the same dose rate are larger than those of
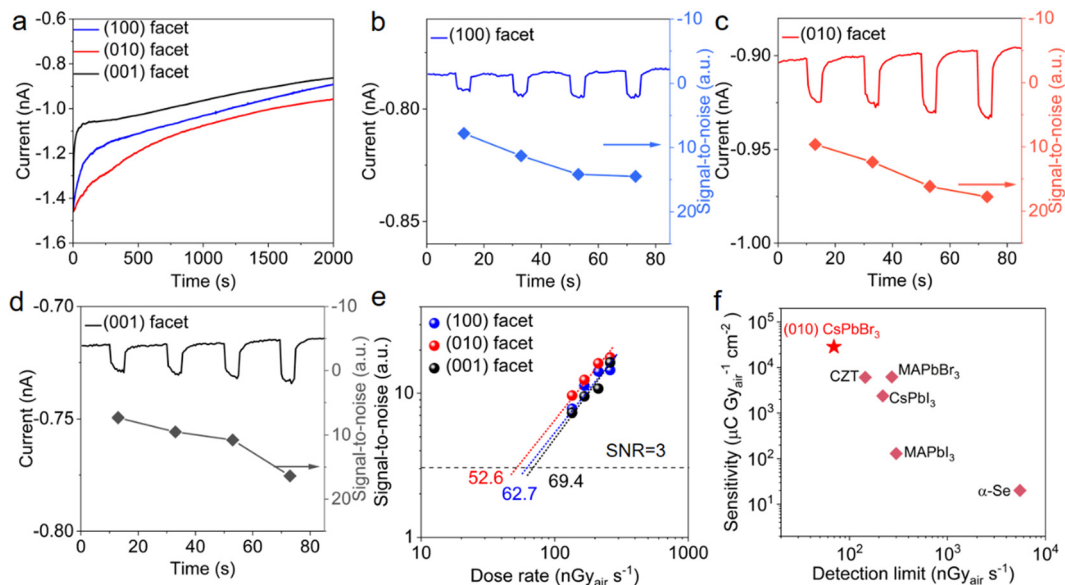
Fig. 5 (a) Comparison of dark current drifts for the (100), (010), and (001) CsPbBr$_3$ crystal detectors under a bias voltage of −10 V. (b−d) Responses and SNR values dependent on X-ray dose rates from 135 to 260 nGy$_{air}$ s^{-1} for the (100), (010), and (001) CsPbBr$_3$ crystal devices when a 2 mm-thick Pb shielding case was inserted between the detector and the X-ray source. (e) Detection limits that are derived from the fitting line with an SNR of 3. (f) Comparison of X-ray detection performance of semiconductor detectors.

Table 1 Comparison of the X-ray detection performance of semiconductors

Device structure	X-ray source (keV)	Electric field (V cm^{-1})	Sensitivity (μC Gy$_{air}^{-1}$ cm^{-2})	Detection limit (nGy$_{air}$ s^{-1})	Ref.
α-Se	20	—	20	5500	2
Au/CZT SC/Au	120	5000	6069	145	29
Au/MAPbI$_3$ SC/Au	100	33	1471.7	46 000	30
Au/CsPbI$_3$ SC/Au	50	41.7	2370	219	31
Au/MAPbBr$_3$ SC/Au	120	150	6169	271	33
Au/FAPbBr$_3$ SC/Au	50	50	130	300	32
EGaIn/(100) CsPbBr$_3$ SC/Au	120	2666	27 638	62.7	This work
EGaIn/(010) CsPbBr$_3$ SC/Au	120	2666	34 449	52.6	This work
EGaIn/(001) CsPbBr$_3$ SC/Au	120	2666	28 421	69.4	This work

the (100) and (001) detectors, indicating a more optimal carrier transport in the (010) wafer.

Fig. 5e compares the detection limits of three wafers, which were derived from the fitting line with an SNR of 3. The (010) device exhibited the lowest detection limit of 52.6 nGy$_{air}$ s^{-1}, which was approximately two orders of magnitude lower than the standard medical diagnostic requirement of 5.5 μGy$_{air}$ s^{-1}.[1] Moreover, the detection limit of our CsPbBr$_3$ SC is two times lower than that of the CZT detector (145 nGy$_{air}$ s^{-1}),[29] and four times lower than that of the CsPbI$_3$ detector (219 nGy$_{air}$ s^{-1}),[31] MAPbBr$_3$ detector (271 nGy$_{air}$ s^{-1}),[33] and FAPbBr$_3$ detector (300 nGy$_{air}$ s^{-1}).[32]

Fig. 5f and Table 1 compare the X-ray detection performance of reported commercial semiconductors and perovskites. It reveals that our (010) facet of the CsPbBr$_3$ SC device displays the highest sensitivity and the lowest detection limit compared to other reported SC devices. Moreover, our CsPbBr$_3$ SC device exhibited long-term stability under ambient conditions for 10 days with negligible change even when the air humidity reached 60% (Fig. S9, ESI†). In summary, the (010) wafer in

CsPbBr$_3$ SC demonstrated optimal X-ray detection properties including high sensitivity, low detection limit, large ion activation energy, and small current drift, providing an approach to optimize X-ray detection devices by controlling the orientations of crystals.

4. Conclusions

We grew CsPbBr$_3$ SCs with the size of Φ 36 mm × 50 mm using a modified Bridgman method. The [100], [010], and [001] orientations of the bulk crystal were determined for X-ray detector fabrication. The structural anisotropy resulted in distinctions in defect densities and charge carrier transport properties. The detector with the [010] orientation of CsPbBr$_3$ SC exhibited a large activation energy (143.77 meV) and ion diffusion barrier energy (0.361 eV), which indicated weak ion migration. The (010) device achieved optimal sensitivity of 34 449 μC Gy$_{air}^{-1}$ cm^{-2} and a detection limit of 52.6 nGy$_{air}$ s^{-1} for 120 keV X-ray detection. Our findings imply that the selection of

This journal is © The Royal Society of Chemistry 2023

J. Mater. Chem. C, 2023, **11**, 9153–9160 | **9159**

the crystal direction is an efficient method for optimizing X-ray radiation detection in perovskite crystals.

Conflicts of interest

There are no conflicts to declare.

Acknowledgements

Notes and references

1 W. Pan, H. Wu, J. Luo, Z. Deng, C. Ge, C. Chen, X. Jiang, W. Yin, G. Niu, L. Zhu, L. Yin, Y. Zhou, Q. Xie, X. Ke, M. Sui and J. Tang, *Nat. Photonics*, 2017, **11**, 726.

2 H. Wu, Y. Ge, G. Niu and J. Tang, *Matter*, 2021, **4**, 144–163.

3 Y. He, M. G. Kanatzidis and I. Hadar, *Nat. Photonics*, 2021, **16**, 14.

4 G. J. Matt, I. Levchuk, J. Knüttel, J. Dallmann, A. Osvet, M. Sytnyk, X. Tang, J. Elia, R. Hock, W. Heiss and C. J. Brabec, *Adv. Mater. Interfaces*, 2020, **7**, 1901575.

5 Y. Hua, F. Cui, P. Zhang, G. Zhang, Q. Zhang and X. Tao, *Z. Anorg. Allg. Chem.*, 2022, **648**, e202200025.

6 X. Li, P. Zhang, Y. Hua, F. Cui, X. Sun, L. Liu, Y. Bi, Z. Yue, G. Zhang and X. Tao, *ACS Appl. Mater. Interfaces*, 2022, **14**, 9340.

7 S. Dong, Z. Hu, P. Wei, J. Han, Z. Wang, J. Liu, B. Su, D. Zhao and Y. Liu, *Adv. Mater.*, 2022, **34**, e2204342.

8 G. Nazir, S. Lee, J. Lee, A. Rehman, J. Lee, S. Seok and S. Park, *Adv. Mater.*, 2022, **34**, e2204380.

9 S. Chu, Y. Zhang, P. Xiao, W. Chen, R. Tang, Y. Shao, T. Chen, X. Zhang, F. Liu and G. Zheng, *Adv. Mater.*, 2022, **34**, e2108939.

10 Y. Zhou, M. Parkes, J. Zhang, Y. Wang, M. Ruddlesden, H. Fielding and L. Su, *Sci. Adv.*, 2022, **8**, eabq8629.

11 Y. He, M. Petryk, Z. Liu, D. G. Chica, I. Hadar, C. Leak, W. Ke, I. Spanopoulos, W. Lin, D. Chung, B. W. Wessels, Z. He and M. G. Kanatzidis, *Nat. Photonics*, 2021, **15**, 36.

12 Q. Fan, H. Xu, S. You, Y. Ma, Y. Liu, W. Guo, X. Hu, B. Wang, C. Gao, W. Liu, J. Luo and Z. Sun, *Small*, 2023, 2301594.

13 C. Li, F. Chen, K. Wang, Q. Yao, J. Zhang, Q. Zhao, Q. Huang, H. Zhu and J. Ding, *J. Mater. Chem. C*, 2022, **10**, 14580.

14 W. Guo, X. Liu, S. Han, Y. Liu, Z. Xu, M. Hong, J. Luo and Z. Sun, *Angew. Chem., Int. Ed.*, 2020, **59**, 13879.

15 P. Zhang, G. Zhang, L. Liu, D. Ju, L. Zhang, K. Cheng and X. Tao, *J. Phys. Chem. Lett.*, 2018, **9**, 5040.

16 F. Chen, C. Li, C. Shang, K. Wang, Q. Huang, Q. Zhao, H. Zhu and J. Ding, *Small*, 2022, **18**, 2203565.

17 R. Toufanian, S. Swain, P. Becla, A. Datta and S. Motakef, *J. Mater. Chem. C*, 2022, **10**, 12708.

18 Y. He, I. Hadar, M. C. De Siena, V. V. Klepov, L. Pan, D. Chung and M. G. Kanatzidis, *Adv. Funct. Mater.*, 2022, **32**, 2112925.

19 L. Pan, Y. He, V. V. Klepov, M. C. De Siena and M. G. Kanatzidis, *IEEE Trans. Med. Imaging*, 2022, **41**, 3053.

20 N. K. Tailor and S. Satapathi, *J. Phys. Chem. C*, 2022, **126**, 17789.

21 M. H. Huang, G. Naresh and H. Chen, *ACS Appl. Mater. Interfaces*, 2018, **10**, 4.

22 C. Tan, S. Hsu, W. Ke, L. Chen and M. H. Huang, *Nano Lett.*, 2015, **15**, 2155.

23 J. Ding, L. Jing, Y. Yuan, J. Zhang, Q. Yao, K. Wang, W. Zhang, H. Sun, B. Liu, T. Zhou and X. Zhan, *ACS Appl. Energy Mater.*, 2020, **3**, 10525.

24 L. Zhang, S. Cui, Q. Guo, C. Ge, Q. Han, Q. Lin, C. Li, X. Zheng, Z. Zhai, L. Wang, Q. Sun, Y. Xu, Y. Liu and X. Tao, *ACS Appl. Mater. Interfaces*, 2020, **12**, 51616.

25 H. Ohshima, *Electrical Phenomena at Interfaces and Bio-interfaces: Fundamentals and Applications in Nano-, Bio-, and Environmental Sciences*, John Wiley & Sons, Inc., 2012, p. 27.

26 B. Zhang, F. Wang, H. Zhang, B. Xiao, Q. Sun, J. Guo, A. B. Hafsia, A. Shao, Y. Xu and J. Zhou, *Appl. Phys. Lett.*, 2020, **116**, 063505.

27 B. Yang, W. Pan, H. Wu, G. Niu, J. Yuan, K. Xue, L. Yin, X. Du, X. Miao, X. Yang, Q. Xie and J. Tang, *Nat. Commun.*, 2019, **10**, 1989.

28 X. Wang, D. Zhao, Y. Qiu, Y. Huang, Y. Wu, G. Li, Q. Huang, Q. Khan, A. Nathan, W. Lei and J. Chen, *Phys. Status Solidi RRL*, 2018, **12**, 1800380.

29 P. Zhang, Y. Hua, Y. Xu, Q. Sun, X. Li, F. Cui, L. Liu, Y. Bi, G. Zhang and X. Tao, *Adv. Mater.*, 2022, **34**, e2106562.

30 X. Geng, H. Zhang, J. Ren, P. He, P. Zhang, Q. Feng, K. Pan, G. Dun, F. Wang, X. Zheng, H. Tian, D. Xie, Y. Yang and T. Ren, *Appl. Phys. Lett.*, 2021, **118**, 063506.

31 B. Zhang, X. Liu, B. Xiao, A. B. Hafsia, K. Gao, Y. Xu, J. Zhou and Y. Chen, *J. Phys. Chem. Lett.*, 2020, **11**, 432.

32 M. Yao, J. Jiang, D. Xin, Y. Ma, W. Wei, X. Zheng and L. Shen, *Nano Lett.*, 2021, **21**, 3947.

33 W. Li, H. Li, J. Song, C. Guo, H. Zhang, H. Wei and B. Yang, *Sci. Bull.*, 2021, **66**, 2199.

34 M. Xia, J. Yuan, G. Niu, X. Du, L. Yin, W. Pan, J. Luo, Z. Li, H. Zhao, K. Xue, X. Miao and J. Tang, *Adv. Funct. Mater.*, 2020, **30**, 1910648.

9160 | *J. Mater. Chem. C*, 2023, **11**, 9153–9160

This journal is © The Royal Society of Chemistry 2023